Multiwavelength Photoacoustic Imaging and Plasmon Resonance Coupling of Gold Nanoparticles for Selective Detection of Cancer

Srivalleesha Mallidi[†], **Timothy Larson**[†], **Justina Tam**[†], **Pratixa P. Joshi**[†], **Andrei Karpiouk**[†], **Konstantin Sokolov**[†,‡], and **Stanislav Emelianov**[*,†]
Department of Biomedical Engineering, University of Texas at Austin, Austin, Texas 78712, and Department of Imaging Physics, University of Texas M.D. Anderson Cancer Center, Houston, Texas 77030

Abstract

Gold nanoparticles targeting epidermal growth factor receptor via antibody conjugation undergo molecular specific aggregation when they bind to receptors on cell surfaces, leading to a red shift in their plasmon resonance frequency. Capitalizing on this effect, we demonstrate the efficacy of the molecular specific photoacoustic imaging technique using subcutaneous tumor-mimicking gelatin implants in ex-vivo mouse tissue. The results of our study suggest that highly selective and sensitive detection of cancer cells is possible using multiwavelength photoacoustic imaging and molecular specific gold nanoparticles.

The developments in the fields of nanotechnology and molecular biology provide a promising platform for detection of cancer at an asymptomatic stage. Bioconjugated nano contrast agents together with imaging techniques can satisfy the compelling need to reliably detect, diagnose and characterize cancer at an early stage.[1–7] Recently, gold nanoparticles (Au NPs) have gained popularity as nano-sized contrast agents[2,6,8–14] for their well-developed bioconjugation protocols,[11,15–17] biocompatibility[18,19] and ease of tuning the optical properties.[20–22] Immunotargeted gold nanoparticles have been used to enhance contrast in optical imaging techniques.[6,9,13,14] However, the penetration depth achievable with high resolution optical imaging techniques is limited to a few millimeters. Optical techniques utilizing incoherent light extend the penetration depth to several centimeters while spatial resolution is severely sacrificed. Therefore, an in vivo imaging technique that is sensitive in detecting Au NPs and capable of imaging deep lying structures is desired. Photoacoustic imaging[23–25] is a technique that can provide penetration depth on the order of centimeters if near-infrared (NIR) laser light is used. In the photoacoustic phenomenon,[26] electromagnetic energy in the form of light is absorbed and subsequently an acoustic wave is emitted. Using a wideband ultrasound detector the acoustic waves can be detected and spatially resolved to provide an image of the optical absorption properties of the internal tissue structure.[23–25]

Gold nanoparticles have been used as contrast agents in photoacoustic imaging because of their unique optical absorption properties.[8,10,27–31] Using three-dimensional (3D) tissue models, we previously demonstrated that highly selective detection of cancer could be achieved using molecular targeted gold nanoparticles and combined photoacoustic and ultrasound imaging.[8,32] In particular, the contrast in the photoacoustic images was attributed to the epidermal growth factor receptor (EGFR)[33,34] mediated assembly of gold nanoparticles in cancerous cells

[*]To whom correspondence should be addressed. Telephone: (512) 471-1733. Fax: (512) 471-0616. emelian@mail.utexas.edu.
[†]University of Texas at Austin.
[‡]University of Texas M.D. Anderson Cancer Center.

leading to plasmon resonance coupling between adjacent gold particles and a red-shift in their absorbance spectra[6,8,9,14] while the nontargeted or isolated gold nanoparticles have absorbance peak at around 520 nm.[8,35,36]

In this paper, we demonstrate the efficacy of multiwavelength photoacoustic imaging in detecting and differentiating cancer cells labeled with anti-EGFR gold nanoparticles from the endogenous chromophores using ex-vivo mouse model of cancer. Four subcutaneous gelatin implants were embedded inside the abdominal region of the ex-vivo mouse tissue. The gelatin implants contained (1) human epithelial carcinoma cells (A431 keratinocyte) labeled with anti-EGFR gold nanoparticles (specifically targeted Au NPs), (2) A431 cells mixed with methoxy-PEG-thiol (mPEG-SH) coated gold nanoparticles (nontargeted Au NPs), (3) untreated A431 cells (control) and (4) NIR absorbing dye (pseudo control for multiwavelength photoacoustic image analysis). Furthermore, we also demonstrated the sensitivity of the molecular specific photoacoustic imaging using 3D tissue models.

The gold nanoparticles used for the gel implants were prepared using citrate reduction of tetrachloroauric (III) acid (HAuCl$_4$) under reflux. The process resulted in 50 nm diameter spherical gold particles. The protocol for antibody conjugation to gold nanoparticles has been described elsewhere.[17] Briefly, the carbohydrate moiety on the Fc region of the Ab was oxidized to an aldehyde by addition of 100 mM NaIO$_4$ to a 1 mg/mL Ab solution in HEPES (1:10 by volume). The Ab was then allowed to react with a hydrazide PEG dithiol heterobifunctional linker (Sensopath Technologies, Inc.), where the hydrazide portion of the linker formed a covalent bond with the aldehyde portion of the Ab, yielding an exposed dithiol moiety that could react strongly with the gold nanoparticles. The Ab-linker was centrifuged in a 100 kD MWCO filter (Amicon) to remove an excess of linker molecules and was resuspended in 40 mM HEPES at pH 8 (5 μg/mL). Then, the Ab-linker was mixed with gold nanoparticles (12 mL, 4×10^{10} particles/mL) at a 1:1 volume ratio and the mixture was allowed to react on a shaker for 30 min at room temperature. Any remaining bare gold surfaces were capped with mPEG-SH (10^{-5} M, 5 kD, Creative PEGWorks) and the particles were washed via centrifugation at 1500 g in the presence of PEG (15 kD, Sigma). The nontargeted gold nanoparticles were prepared by reacting gold nanoparticles (12 mL, 4×10^{10} particles/mL) with mPEG-SH (1.2 mL, 10^{-5} M). The resulting PEGylated particles were also washed in the presence of PEG via centrifugation at 1500 g. The targeted and nontargeted gold nanoparticles were sterile filtered (0.2 μm pore size, Corning) before being mixed with cells.

The targeted, nontargeted, and untreated samples contained 4.4×10^6 cells/mL each. After centrifugation, targeted gold nanoparticles were resuspended in 12 mL of phenol-free DMEM (Invitrogen) at a concentration of 4×10^{10} particles/mL. They were incubated with cells for 30 min at room temperature on a shaker. The cells and particles were then centrifuged at 110 g for 3 min and unbound particles in the supernatant were discarded. Cell samples containing either PEGylated gold nanoparticles mixed with cells or cells alone were prepared in phenol-free DMEM.

The specifically targeted, nontargeted, and control cells were resuspended in 500 μL of gelatin (Sigma) solution (10% by weight). In addition, 20 μM NIR dye (ADS 740WS, American Dye Source) solution was also prepared with gelatin (10% by weight). To achieve ultrasonic scattering, 0.4% (by weight) 15 μm diameter silica particles (Sigma) were added to the dye solution. The dye was used as a pseudo control for multiwavelength photoacoustic image analysis. The four gelatin suspensions were maintained at about 37 °C. Approximately 400 μL of each gelatin solution was used for subcutaneous injections and the remaining 100 μL of gelatin solutions were used to measure optical spectra (Figure 1) with a spectrophotometer (BioTek Synergy HT microtiter plate reader). The extinction spectra of A431 cells labeled with anti-EGFR Au NPs and A431 cells mixed with mPEG-SH coated Au NPs were normalized

with respect to the extinction spectrum of untreated A431 cells (control). As expected, the cells specifically targeted with gold nanoparticles (solid red line) have the peak red-shifted and broadened due to EGFR-mediated aggregation of gold nanoparticles,[6,8,9,14] while the nontargeted gold nanoparticles have an absorbance peak near 520 nm (dotted green line). The pseudo control ADS 740WS dye solution has an absorbance peak at 740 nm (dashed blue line) in agreement with the manufacturer specifications.

A mouse euthanized for other research purposes was obtained from the Animal Resource Center at the University of Texas at Austin. A commercially available depilatory solution was used to remove hair from the abdominal region of the mouse. The gelatin suspensions were injected under the skin of the mouse to mimic subcutaneous tumors. A 27-gauge needle syringe was used for the subcutaneous implantation of 400 μL of gelatin suspensions. The colder environment of the mouse carcass facilitated the hardening of the gelatin under the skin. In Figure 2, the gelatin implants containing the cells with targeted Au NPs and the A431 cells mixed with mPEG-SH coated Au NPs are shown in the red and green insets respectively. The two control gelatin implants containing untreated A431 cells and ADS740WS dye are shown in the white and blue insets respectively. The tumor mimicking gelatin implants in the mouse ex-vivo tissue were approximately 6–8 mm in diameter.

The photoacoustic and ultrasound images from the same cross section of the abdomen region of the mouse were obtained using the experimental setup shown in Figure 3. The imaging system consists of a microprocessor unit with a custom built LabVIEW application that controls the ultrasound pulser/receiver, pulsed laser, data acquisition unit, and all motion axes needed for 3D mechanical scanning.[25,37] A 25 MHz single element focused (focal depth = 25.4 mm, $f\# = 4$) ultrasound transducer was used to obtain both ultrasound and photoacoustic images. Either a Q-switched Nd:YAG laser (5 ns pulses, 20 Hz pulse repetition frequency) or a tunable OPO laser system (7 ns pulses, 10 Hz pulse repetition frequency) were used to generate photoacoustic transients. The laser irradiation was delivered via optical fiber bundle consisting of 600 μm diameter fibers. On the proximal end of the bundle, seven fibers arranged in a circular configuration were coupled to a laser beam using appropriate focusing optics. On the distal end, the fibers were attached to the transducer such that the foci of the ultrasound transducer and the optical fiber bundle spatially coincide. This integrated probe consisting of the ultrasound transducer and the optical fiber bundle was attached to the motion axis to facilitate the scanning of the ex-vivo mouse tissue. The 2D photoacoustic and ultrasound images were obtained by mechanically scanning over the desired region with 100 μm lateral steps to satisfy Nyquist sampling criterion. At each step, the pulsed laser light irradiated the tissue and the trigger signal from the laser source initiated the data acquisition performed by an 8-bit, 500 MS/s digitizer. The same trigger signal, delayed by several microseconds, was sent to the pulser/receiver to initiate the pulse-echo ultrasound imaging. Therefore, a captured A-line contained spatially coregistered photoacoustic signal and the conventional ultrasound radio frequency (RF) data separated by the user defined delay.[25,37] The combined ultrasound and photoacoustic imaging was repeated for multiple laser wavelengths (532 nm, 680–860 nm in steps of 20 nm) at the same imaging cross-section of the ex-vivo mouse tissue.

During the offline processing, the photoacoustic and ultrasound signals were extracted from the A-line records obtained at each lateral step of the mechanical scan. A digital bandpass (5–45 MHz) filter was applied to these raw RF signals to reduce noise. The ultrasound and photoacoustic analytic signals were obtained by applying the Hilbert transform on the filtered RF data. The absolute values of the photoacoustic analytic signals obtained at various wavelengths were normalized to compensate for the wavelength dependent laser fluence output. Further, the photoacoustic signals were also corrected for the depth dependent attenuation of laser fluence using exponential compensation curves. The compensation curves were calculated using Monte Carlo (MC) simulations[38] for various laser illumination

wavelengths. Since the gelatin implants were subcutaneous, a simple two layer model with skin and scattering medium was considered for MC simulations as shown in Figure 4a. The thickness of the skin layer, measured from the ultrasound image of the ex-vivo mouse tissue, was about 0.8 mm. The thickness of the second layer used in the MC simulation was 20 mm. The optical properties (absorption and scattering coefficients, anisotropy and index of refraction) of skin[39–41] and the cell suspension medium[42] were obtained from literature. The depth-resolved fluence obtained from the MC simulations for different wavelength illuminations is shown in Figure 4b. The graphs in Figure 4b clearly indicate the wavelength-dependent change in fluence with depth. The optical absorption coefficient for the second layer was considered to be wavelength independent to enable relative comparison of the fluence compensated photoacoustic signals and the optical absorption properties of the subcutaneous gelatin implants from spectrophotometer. Finally, the compensated photoacoustic data was spatially interpolated and displayed using the same dynamic range.

The ultrasound and photoacoustic images obtained at multiple wavelengths (532, 680, 740, 800, and 860 nm) are presented in Figure 5. The ultrasound image clearly shows the mouse skin as the hyperechoic region and the subcutaneous gelatin implants as the hypoechoic regions. The regions of gelatin implant with EGFR targeted Au NPs, PEGylated Au NPs, control A431 cells, and the ADS 740WS dye are encircled in red, green, white, and blue insets, respectively. As expected, the gelatin implant with control A431 cells (white inset) does not produce any photoacoustic signal while the cells mixed with PEGylated Au NPs (green inset) produce photoacoustic signal only at 532 nm laser irradiation. The intensity of the photoacoustic transients produced by the cells labeled with EGFR targeted Au NPs (red inset) decreases as a function of wavelength in congruence with the optical absorption properties of these cells shown in Figure 1. The photoacoustic image at 740 nm (Figure 5d) clearly has greater photoacoustic signal intensity in the region of the gelatin implant with dye. Indeed, the ADS740WS dye used as a pseudo control has an absorption peak at 740 nm. Therefore, the multiwavelength photoacoustic images qualitatively indicate the spectral variations in the optical absorption properties of the gelatin implants.

The optical absorption properties of tissue components can be quantitatively determined by analysis of the spectral variation in the generated photoacoustic transients. For example, multi-wavelength photoacoustic imaging was used to differentiate atherosclerotic plaques,[43] to determine blood oxygenation saturation,[44] and the distribution of exogenous contrast agents. [45] In addition to the analysis of the characteristics of the generated photoacoustic transients to gauge the spectral properties of the gelatin implants, we also performed intraclass correlation analysis[46–50] to measure the agreement between the optical properties of the gelatin implants obtained from the spectrophotometer and the photoacoustic signals. This method aided in quantitatively differentiating the specifically targeted Au NPs and nontargeted Au NPs.

Intraclass correlation is a method employed in assessing agreement between different observers or different methods when used on the same set of subjects. A correlation coefficient value greater than 0.75 indicates a good agreement between the two methods.[46,50] To obtain the optical absorption spectrum of a particular pixel in the multiwavelength photoacoustic image stack, the sum of the photoacoustic signal amplitude in a kernel (500 μm laterally and 300 μm axially) around the pixel was calculated and analyzed as a function of wavelength. The dimensions of the kernel were chosen according to the lateral and axial resolution of the photoacoustic image. The normalized spectrum of the pixel, obtained from the photoacoustic signals, was then compared individually to the targeted, nontargeted, and dye optical spectra obtained from the spectrophotometer using intraclass correlation analysis. The procedure was repeated for every pixel in the photoacoustic image stack and the resulting correlation coefficients were formed into an image with correlation values in the range of −1 (negative agreement) to +1 (positive agreement). The ultrasound images overlaid with correlation

coefficient images with a threshold value of 0.75 are shown in Figure 6. Clearly, the correlation analysis between multiwavelength photoacoustic images and spectrum of the targeted Au NPs produced a good correlation coefficient only in the region with the gelatin implant containing cells with targeted Au NPs (Figure 5a). Similar trend can also be noticed with the gelatin implant containing ADS740WS dye (Figure 5c). The spectrum of the nontargeted Au NPs also well correlated with multiwavelength photoacoustic signals from the regions outside of the gelatin implant with nontargeted Au NPs (Figure 5b). This is more likely due to chromophores, such as hemoglobin in blood, having higher optical absorption at 532 nm and lower absorption in the 680–860 nm wavelength range. However, the optical absorption spectrum of blood in 532–600 nm range is not monotonic compared to spectra of gold nanoparticles and, therefore, additional measurement at intermediate (e.g., 575 nm) wavelength could discriminate the blood from nontargeted Au NPs. In addition, multiwavelength photoacoustic images before and after the injection of Au NPs can be performed to identify regions with blood.

The graphical comparison of the photoacoustic spectra and optical spectra from spectrophotometer of the gelatin implants is shown in Figure 7. The photoacoustic spectra of the gelatin implants were obtained by calculating the sum of the photoacoustic signal amplitudes at pixels with correlation coefficient greater than 0.75. The normalized optical spectra obtained from the spectrophotometer and the photoacoustic spectra are represented by a solid black line and data points, respectively. The error bars in Figure 7 represent the standard deviation in the photoacoustic signal amplitude in the region of interest. Clearly, the graphs indicate a good agreement between the photoacoustic spectra and the optical spectra of the specifically targeted Au NPs, nontargeted Au NPs and the ADS740WS NIR dye. The multiwavelength photoacoustic images in Figure 5 (red and green insets) qualitatively show the difference between the targeted Au NPs and nontargeted Au NPs whereas the graphs in Figure 7a,b quantitatively represent the difference in optical absorption properties of the gelatin implants. As expected, the quantitative analysis of photoacoustic signals obtained from the gelatin implant with NIR absorbing ADS 740WS dye (pseudo control) shown in Figure 7c depicts the dye has an absorption peak at 740 nm. Our results clearly indicate the feasibility of applying multiwavelength photoacoustic imaging to qualitatively and quantitatively differentiate EGFR targeted Au NPs and nontargeted Au NPs.

It is imperative to estimate the sensitivity of the molecular specific photoacoustic imaging technique in tissue mimicking phantoms prior to conducting in vivo experiments; that is, the minimum concentration of labeled cells or Au NPs required to observe photoacoustic transients needs to be determined. For this study, tissue-mimicking models were used. The tissue models were made with gelatin containing different concentrations of human epithelial carcinoma cells (A431 keratinocyte) labeled with anti-EGFR Au NPs. Specifically, cells labeled with anti-EGFR Au NPs were prepared at a 1×10^7 cells/mL concentration using the procedure described previously for ex-vivo mouse tissue experiments. The cell suspension was mixed with different volumes of gelatin solution (10% by weight) to obtain various concentrations of cells labeled with Au NPs. The cell/gelatin solutions (100 μL) were pipetted into separate wells for imaging experiments. The ultrasound and multiwavelength photoacoustic imaging of the cell/gelatin solutions was performed using an integrated probe consisting of 25 MHz single element transducer and optical fiber bundle as shown in Figure 3. After the imaging experiments, the cell/gelatin samples were extracted from the wells and dissolved in 1% nitric acid for quantitative determination of Au NPs concentration using inductively coupled plasma mass spectroscopy (ICP-MS).

The ultrasound and photoacoustic images of the cell/gelatin samples with anti-EGFR Au NPs labeled cells are shown in Figure 8. The photoacoustic images shown in Figure 8 were obtained at 680 nm wavelength illumination. The concentration of cells and the Au NPs concentration obtained from ICP-MS analysis of the respective gelatin samples are also shown in Figure 8.

A decrease in the amplitude of the backscattered echo in ultrasound images (Figure 8a–e) clearly indicates a decrease in the concentration of cells in the gelatin samples. It can also be observed that the photoacoustic signal amplitude (Figure 8f–j) decreases as a function of cell/Au NPs concentration.

The change in the photoacoustic signal amplitude in relation to the concentration of Au NPs is quantitatively demonstrated in Figure 9. Specifically, a 2 mm × 1 mm region of interest (ROI) was chosen for each cell/gelatin sample image (Figure 8f–j) and divided into subareas measuring 0.5 mm × 0.5 mm. The mean and the standard deviation of the photoacoustic signal amplitude in the subareas was calculated and plotted as a function of Au NPs concentration in Figure 9. A linear regression fit of the data yielded an R^2 value equal to 0.995. This result was expected; given the constant laser input fluence, the amplitude of the photoacoustic signal is proportional to absorber (Au NPs) concentration. From our experiments, the limit of detection for the photoacoustic imaging technique was ~3.1×10^4 cells/mL or ~2.94×10^7 Au NPs/mL. It is to be noted that the experiments were performed at fluence of 5 mJ/cm^2; this value is less than ANSI standard of the maximum allowable fluence (20 mJ/cm^2) for pulsed lasers.[24]

Photoacoustic imaging provides functional information of subsurface structures with ultrasonic resolution. The caveat in obtaining high resolution photoacoustic images with a single element, high frequency ultrasound transducer is that the photoacoustic images cannot be obtained in real time. The mechanical scanning of the single element transducer and the pulse repetition rate of the laser affect the time taken to acquire the combined ultrasound and photoacoustic images of the ex-vivo mouse tissue. The current experimental setup can be improved to obtain real-time photoacoustic images with the use of array transducers or a high pulse repetition rate laser. Moreover, the synergistic combination of ultrasound and photoacoustic imaging provides functional information such as the distribution of nanoparticles in the context of structural information. The combined ultrasound and photoacoustic imaging together with molecular specific gold nanoparticles can be used to detect cancer at an asymptomatic stage and can also be used to accurately plan and guide the photothermal therapeutic procedures and monitor the outcome.[51–53]

In conclusion, we have demonstrated in ex-vivo mouse tissue that multiwavelength photoacoustic imaging can detect cancer with high selectivity and sensitivity based on the plasmon-resonance coupling effect of the EGFR targeted Au NPs. Intraclass correlation analysis was performed to quantitatively differentiate the specifically targeted Au NPs and nontargeted Au NPs. The agreement between the photoacoustic spectrum of the ADS740WS dye and the spectrophotometer data further supported the results of the quantitative analysis performed on the multiwave length photoacoustic images. We also determined sensitivity of photoacoustic imaging technique in detecting Au NPs using tissue mimicking samples. Finally based on our results presented in this paper, further investigations will be designed and implemented on murine tumor models to determine minimum concentration of specifically targeted gold nanoparticles required to obtain sufficient contrast in photoacoustic images from the deeply embedded tumors.

Acknowledgments

References

1. Pope-Harman A, Cheng MM, Robertson F, Sakamoto J, Ferrari M. Med Clin North Am 2007;91(5): 899–927. [PubMed: 17826110]

2. Sharma P, Brown S, Walter G, Santra S, Moudgil B. Adv Colloid Interface Sci 2006;123–126:471–85.

3. Sunderland CJ, Steiert M, Talmadge JE, Derfus AM, Barry SE. Drug Dev Res 2006;67:70–93.

4. Weissleder R, Mahmood U. Radiology 2001;219(2):316–33. [PubMed: 11323453]

5. Wickline SA, Lanza GM. Circulation 2003;107(8):1092–5. [PubMed: 12615782]

6. Sokolov K, Follen M, Aaron J, Pavlova I, Malpica A, Lotan R, Richards-Kortum R. Cancer Res 2003;63:1999–2004. [PubMed: 12727808]

7. Anker JN, Hall WP, Lyandres O, Shah NC, Zhao J, Van Duyne RP. Nat Mater 2008;7(6):442–453. [PubMed: 18497851]

8. Mallidi S, Larson T, Aaron J, Sokolov K, Emelianov S. Opt Express 2007;15:6583–6588. [PubMed: 19546967]

9. Aaron JS, Nitin N, Travis K, Kumar S, Collier T, Park SY, José-Yacamán M, Coghlan L, Follen M, Richards-Kortum R, Sokolov KV. J Biomed Opt 2007;12:034007. [PubMed: 17614715]

10. Copland JA, Eghtedari M, Popov VL, Kotov N, Mamedova N, Motamedi M, Oraevsky AA. Mol Imaging Biol 2004;6:341–349. [PubMed: 15380744]

11. Hainfeld JF, Slatkin DN, Focella TM, Smilowitz HM. Br J Radiol 2006;79(939):248–53. [PubMed: 16498039]

12. Khlebtsov B, Zharov V, Melnikov A, Tuchin V, Khlebtsov N. Nanotechnology 2006;17:5167–5179.

13. Loo C, Lin A, Hirsch L, Lee MH, Barton J, Halas N, West J, Drezek R. Technol Cancer Res Treat 2004;3(1):33–40. [PubMed: 14750891]

14. Sokolov K, Aaron J, Hsu B, Nida D, Gillenwater A, Follen M, MacAulay C, Adler-Storthz K, Korgel B, Descour M, Pasqualini R, Arap W, Lam W, Richards-Kortum R. Technol Cancer Res Treat 2003;2:491–504. [PubMed: 14640761]

15. Hermanson, GT. Bioconjugate techniques. Academic; San Diego, CA: 1996.

16. Horisberger M. Scanning Electron Microsc 1981;2:9–31.

17. Kumar S, Aaron J, Sokolov K. Nat Protoc 2008;3(2):314–20. [PubMed: 18274533]

18. Hayat, M. Colloidal gold: Principles, methods and aapplications. Academic; San Diego, CA: 1989.

19. Connor EE, Mwamuka J, Gole A, Murphy CJ, Wyatt MD. Small 2005;1(3):325–7. [PubMed: 17193451]

20. Oldenburg SJ, Averitt RD, Westcott SL, Halas NJ. Chem Phys Lett 1998;288(2–4):243–247.

21. Oldenburg SJ, Jackson JB, Westcott SL, Halas NJ. Appl Phys Lett 1999;75:2897–2899.

22. Yguerabide J, Yguerabide EE. J Cell Biochem 2001;84(S37):71–81.

23. Oraevsky, A.; Karabutov, A. Optoacoustic Tomography. In: Vo-Dinh, T., editor. Biomedical Photonics Handbook. Vol. PM125. CRC Press; Boca Raton, FL: 2003. p. 34/1-34/34.Chapter 34

24. Xu M, Wang LV. Rev Sci Instrum 2006;77(4):041101.

25. Emelianov, SY.; Aglyamov, SR.; Karpiouk, AB.; Mallidi, S.; Park, S.; Sethuraman, S.; Shah, J.; Smalling, RW.; Rubin, JM.; Scott, WG. In: Yuhas, MP., editor. Synergy and applications of combined ultrasound, elasticity, and photoacoustic imaging; Proceedings of the IEEE International Ultrasonics Symposium; Vancouver, Canada. October 3–6, 2006; Institute of Electrical and Electronics Engineers; 2006. p. 405-415.

26. Bell AG. Am J Sci 1880;20:305–324.

27. Wang, B.; Yantsen, E.; Larson, T.; Sethuraman, S.; Sokolov, K.; Emelianov, S. In: Yuhas, MP., editor. Intravascular Photoacoustic Imaging with Gold Nanoparticles; Proceedings of the 2007 IEEE Ultrasonics Symposium; New York, NY. 2007; Institute of Electrical and Electronics Engineers; 2007. p. 848-851.

28. Kim K, Huang SW, Ashkenazi S, O'Donnell M, Agarwal A, Kotov NA, Denny MF, Kaplan MJ. Appl Phys Lett 2007;90(22):223901.

29. Eghtedari M, Oraevsky A, Copland JA, Kotov NA, Conjusteau A, Motamedi M. Nano Lett 2007;7 (7):1914–1918. [PubMed: 17570730]

30. Yang X, Skrabalak SE, Li ZY, Xia Y, Wang LV. Nano Lett 2007;7(12):3798–3802. [PubMed: 18020475]

31. Li PC, Huang SW, Wei CW, Chiou YC, Chen CD, Wang CRC. Opt Lett 2005;30(24):3341–3343. [PubMed: 16389825]

32. Emelianov, S.; Mallidi, S.; Larson, T.; Sokolov, K. Photoacoustic Imaging and Therapy Utilizing Molecular Specific Plasmonic Nanoparticles. In: Wang, LV., editor. Photoacoustic Imaging and Spectroscopy. CRC; Boca Raton, FL: 2009.

33. Barnes, C.; Kumar, R. Biology of the Epidermal Growth Factor Receptor Family. In: Kumar, R., editor. Molecular Targeting and Signal Transduction. Springer; New York: 2004. p. 1-13.

34. Todd R, Wong DTW. Histol Histopathol 1999;14:491–500. [PubMed: 10212811]

35. Bohren, CF.; Huffman, DR. Absorption and scattering of light by small particles. Wiley-VCH; Berlin: 1983. p. 3166

36. Jain PK, Lee KS, El-Sayed IH, El-Sayed MA. J Phys Chem 2006;110:7238–7248.

37. Mallidi, S.; Aglyamov, SR.; Karpiouk, AB.; Park, S.; Emelianov, SY. In: Emelianov, S.; Walker, WF., editors. Functional and morphological ultrasonic biomicroscopy for tissue engineers; Proceedings of the SPIE Medical Imaging: Ultrasonic Imaging and Signal Processing; San Diego, CA. February 11–16, 2006; Bellingham, WA: SPIE; 2006. p. 61470Y1-7.

38. Wang LH, Jacques SL, Zheng LQ. Comput Methods Programs Biomed 1995;47:131–146. [PubMed: 7587160]

39. Bashkatov AN, Genina EA, Kochubey VI, Tuchin VV. J Phys D: Appl Phys 2005;38(15):2543.

40. Jacques, SL. Skin Optics. [accessed May, 2008]. http://omlc.ogi.edu/news/jan98/skinoptics.html

41. Simpson CR, Kohl M, Essenpreis M, Cope M. Phys Med Biol 1998;43(9):2465–2478. [PubMed: 9755939]

42. Mourant JR, Freyer JP, Hielscher AH, Eick AA, Shen D, Johnson TM. Appl Opt 1998;37(16):3586–93. [PubMed: 18273328]

43. Sethuraman S, Amirian JH, Litovsky SH, Smalling RW, Emelianov SY. Opt Express 2008;16(5):3362–7. [PubMed: 18542427]

44. Zhang HF, Maslov K, Stoica G, Wang LV. Nat Biotechnol 2006;24(7):848–51. [PubMed: 16823374]

45. Razansky D, Vinegoni C, Ntziachristos V. Opt Lett 2007;32(19):2891–3. [PubMed: 17909608]

46. Bartko JJ. Psychol Rep 1966;19(1):3–11. [PubMed: 5942109]

47. Bland JM, Altman DG. Comput Biol Med 1990;20(5):337–40. [PubMed: 2257734]

48. Kuo BI. Circulation 1994;89(4):1910–1. [PubMed: 8149563]

49. Muller R, Buttner P. Stat Med 1994;13(23–24):2465–76. [PubMed: 7701147]

50. Indrayan, A.; Sarmukaddam, SB. Medical biostatistics. CRC Press; Boca Raton, FL: 2001.

51. Larina IV, Larin KV, Esenaliev RO. J Phys D: Appl Phys 2005;(15):2633.

52. Shah J, Aglyamov SR, Sokolov K, Milner TE, Emelianov SY. Opt Express 2008;16(6):3776–3785. [PubMed: 18542473]

53. Shah J, Park S, Aglyamov S, Larson T, Ma L, Sokolov K, Johnston K, Milner TE, Emelianov SY. J Biomed Opt 2008;13(3):034024. [PubMed: 18601569]
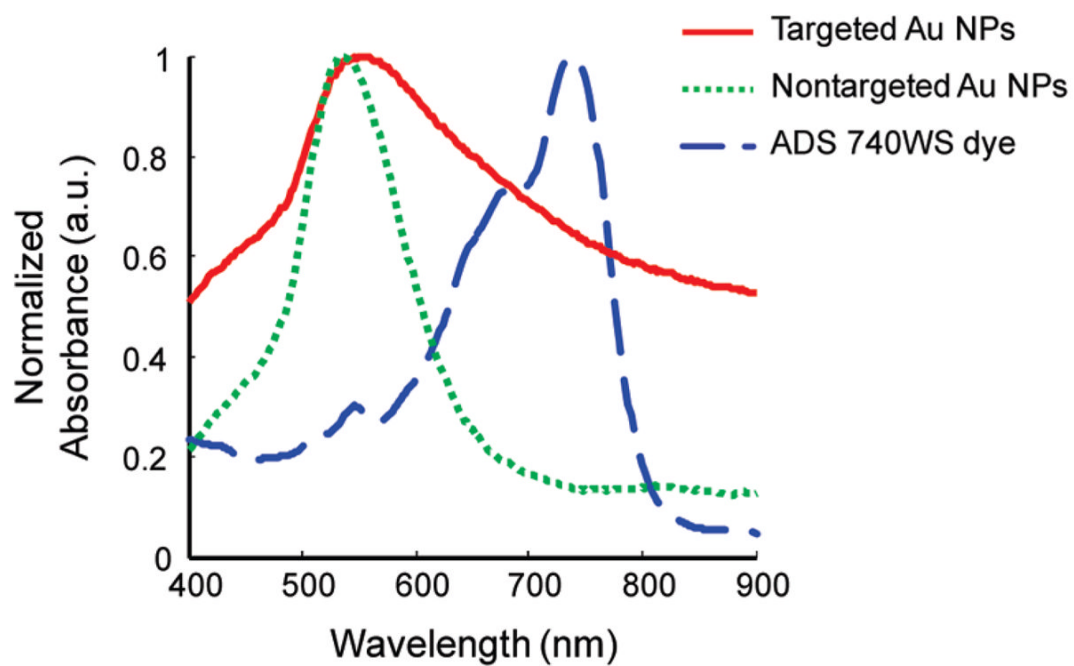
Figure 1.
Normalized absorbance spectra of A431 cells labeled with anti-EGFR Au NPs (solid red line), A431 cells mixed with mPEG-SH coated Au NPs (dotted green line), and ADS740WS dye (dashed blue line).
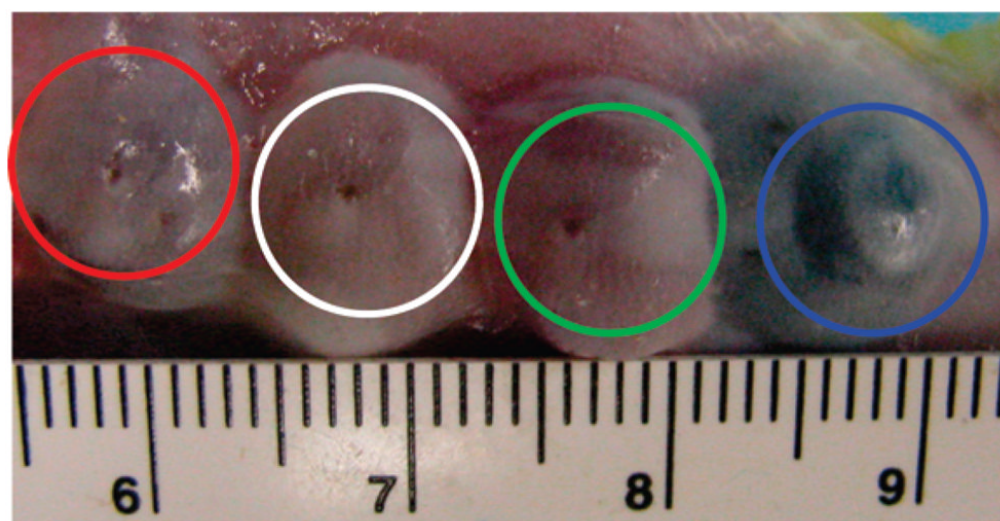
Figure 2.
Photograph of the subcutaneous gelatin implants in mouse tissue ex-vivo. The gelatin implants containing the cells with targeted Au NPs, control A431 cells, A431 cells mixed with mPEG-SH coated Au NPs and NIR dye are shown in red, white, green, and blue insets respectively.
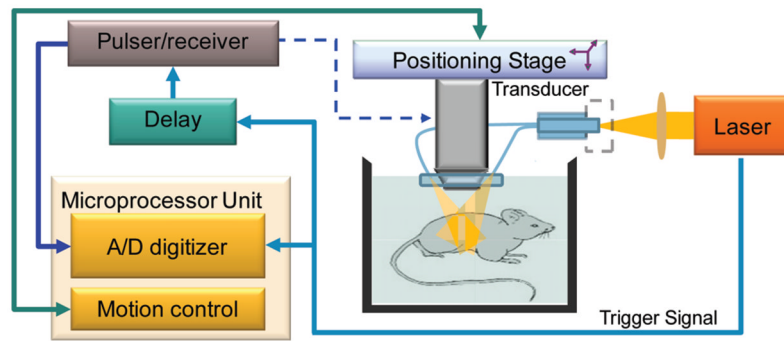
Figure 3.
Block diagram of the combined ultrasound and photoacoustic imaging system.
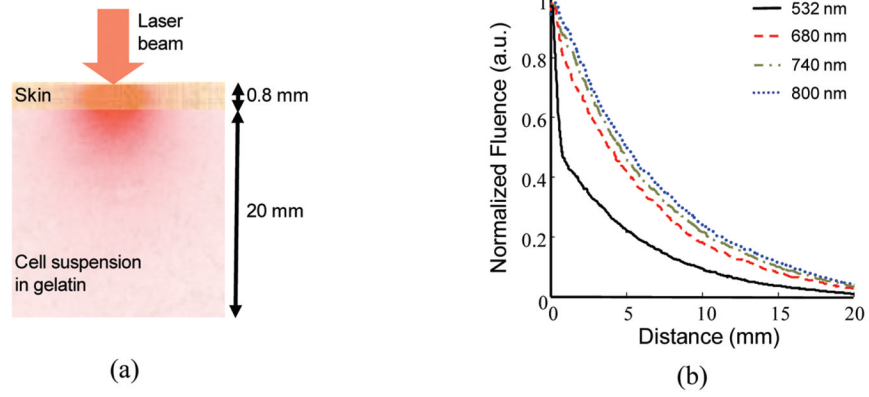
Figure 4.
(a) Schematic representation of the two layer model used for MC simulations of mouse skin and underlying tissue. (b) The depth resolved fluence obtained from the MC simulations for different wavelength illumination.
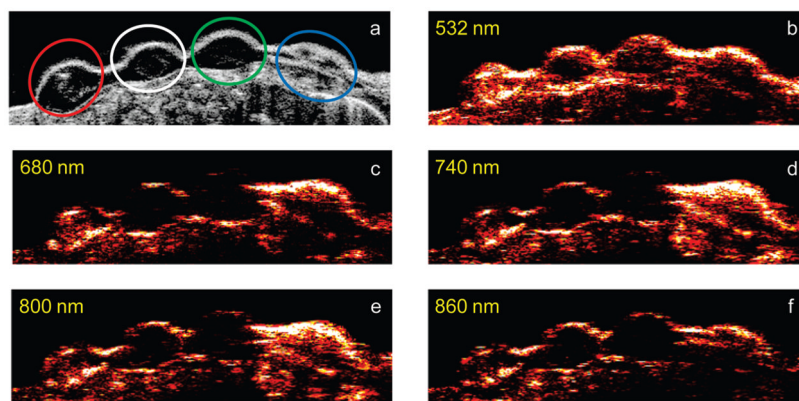
Figure 5.
Ultrasound (a) and photoacoustic (b–f) images of gelatin implants in mouse tissue ex-vivo at laser illumination wavelength 532, 680, 740, 800, and 860 nm, respectively. The gelatin implants containing the cells with targeted Au NPs, control A431 cells, the A431 cells mixed with mPEG-SH coated Au NPs, and NIR dye are shown on the ultrasound image in red, white, green, and blue insets, respectively. The images measure 44 mm laterally and 11 mm axially.
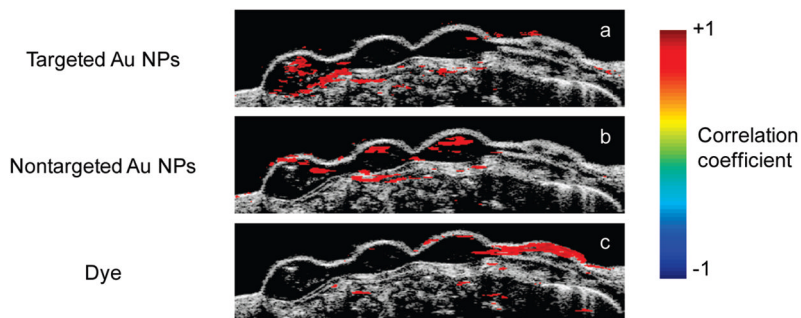
Figure 6.
Correlation coefficient images overlaid on ultrasound image of the subcutaneous gelatin implants in mouse tissue ex-vivo. The correlation coefficient images were obtained by comparing multiwavelength photoacoustic images with optical spectra of (a) targeted Au NPs, (b) nontargeted Au NPs and (c) ADS740WS dye. Only correlation coefficient values greater than 0.75 are displayed in the images. The images measure 44 mm laterally and 9.1 mm axially.
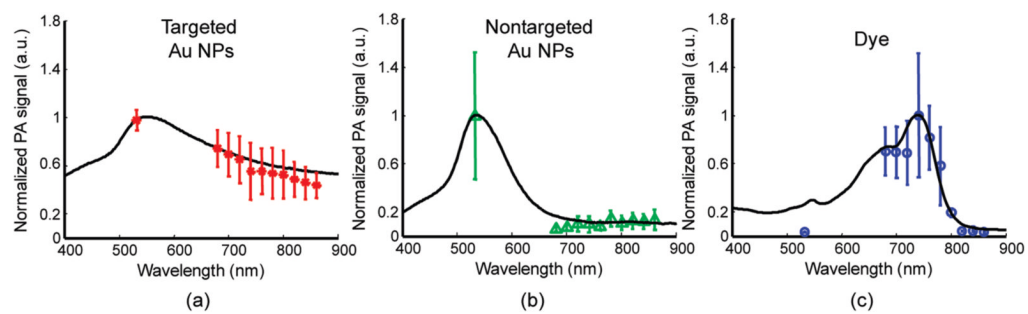
Figure 7.
Comparison of absorption spectrum of (a) targeted Au NPs, (b) nontargeted Au NPs, and (c) ADS740WS dye obtained from multiwavelength photoacoustic images (data points) and spectrophotometer (solid line).
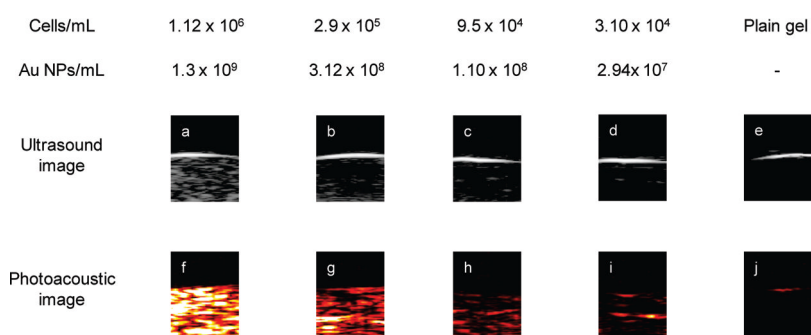
Cells/mL	1.12×10^6	2.9×10^5	9.5×10^4	3.10×10^4	Plain gel
Au NPs/mL	1.3×10^9	3.12×10^8	1.10×10^8	2.94×10^7	-
Ultrasound image	a	b	c	d	e
Photoacoustic image	f	g	h	i	j

Figure 8.
The ultrasound and photoacoustic images of cell/gelatin samples at different cell concentration. The photoacoustic images were obtained at 680 nm wavelength illumination. The images represent a 2 mm × 2.5 mm field of view.
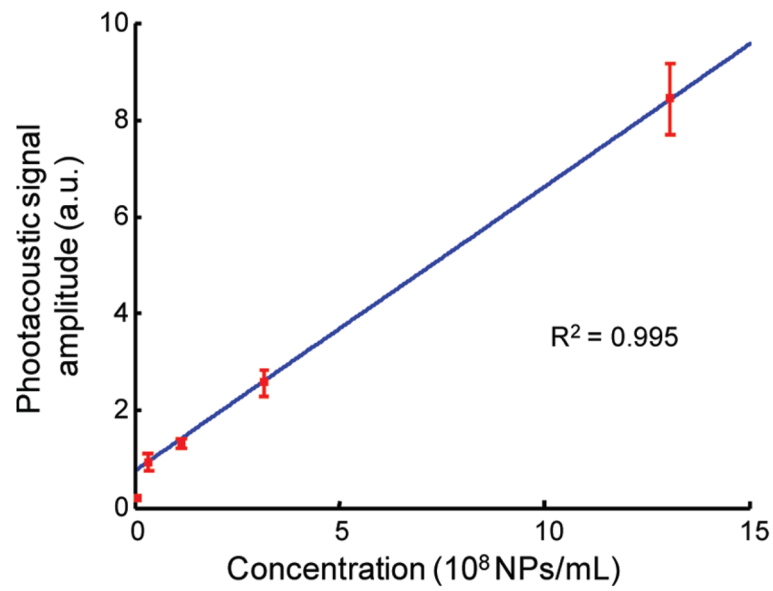
Figure 9.
Graph depicting the change in photoacoustic signal amplitude with Au NPs concentration. The solid line represents the linear regression fit of the data with R^2 equal to 0.995.